Biomedical Optics EXPRESS

In vivo dual-modality photoacoustic and optical coherence tomography imaging of human dermatological pathologies

Behrooz Zabihian,[1] Jessika Weingast,[2] Mengyang Liu,[1] Edward Zhang,[3] Paul Beard,[3] Hubert Pehamberger,[2] Wolfgang Drexler,[1,*] and Boris Hermann[1]

[1]*Center for Medical Physics and Biomedical Engineering, Medical University of Vienna, AKH 4L, Währinger Gürtel 18-20, Vienna 1090, Austria*
[2]*Department of Dermatology, Medical University of Vienna, Währinger Gürtel 18-20, Vienna 1090, Austria*
[3]*Department of Medical Physics & Biomedical Engineering, University College London, Gower Street, London, UK*
[*]*wolfgang.derxler@meduniwien.ac.at*

Abstract: Vascular abnormalities serve as a key indicator for many skin diseases. Currently available methods in dermatology such as histopathology and dermatoscopy analyze underlying vasculature in human skin but are either invasive, time-consuming, and laborious or incapable of providing 3D images. In this work, we applied for the first time dual-modality photoacoustic and optical coherence tomography that provides complementary information about tissue morphology and vasculature of patients with different types of dermatitis. Its noninvasiveness and relatively short imaging time and the wide range of diseases that it can detect prove the merits of the dual-modality imaging system and show the great potential of its clinical use in the future.

OCIS codes: (170.4500) Optical coherence tomography; (170.5120) Photoacoustic imaging; (170.3880) Medical and biological imaging; (170.1870) Dermatology.

References and links

1. H. Kittler, H. Pehamberger, K. Wolff, and M. Binder, "Diagnostic accuracy of dermoscopy," Lancet Oncol. **3**(3), 159–165 (2002).
2. C. Blatter, J. Weingast, A. Alex, B. Grajciar, W. Wieser, W. Drexler, R. Huber, and R. A. Leitgeb, "In situ structural and microangiographic assessment of human skin lesions with high-speed OCT," Biomed. Opt. Express **3**(10), 2636–2646 (2012).
3. B. J. Vakoc, D. Fukumura, R. K. Jain, and B. E. Bouma, "Cancer imaging by optical coherence tomography: preclinical progress and clinical potential," Nat. Rev. Cancer **12**(5), 363–368 (2012).
4. E. Laistler, R. Loewe, and E. Moser, "Magnetic resonance microimaging of human skin vasculature in vivo at 3 Tesla," Magn. Reson. Med. **65**(6), 1718–1723 (2011).
5. W. Drexler and F. G. James, *Optical Coherence Tomography, Technology and Applications* (Springer, 2008).
6. A. Alex, B. Považay, B. Hofer, S. Popov, C. Glittenberg, S. Binder, and W. Drexler, "Multispectral in vivo three-dimensional optical coherence tomography of human skin," J. Biomed. Opt. **15**(2), 026025 (2010).
7. W. Drexler, M. Liu, A. Kumar, T. Kamali, A. Unterhuber, and R. A. Leitgeb, "Optical coherence tomography today: speed, contrast, and multimodality," J. Biomed. Opt. **19**(7), 071412 (2014).
8. A. Alex, J. Weingast, M. Weinigel, M. Kellner-Höfer, R. Nemecek, M. Binder, H. Pehamberger, K. König, and W. Drexler, "Three-dimensional multiphoton/optical coherence tomography for diagnostic applications in dermatology," J. Biophotonics **6**(4), 352–362 (2013).
9. J. Qin, J. Jiang, L. An, D. Gareau, and R. K. Wang, "In vivo volumetric imaging of microcirculation within human skin under psoriatic conditions using optical microangiography," Lasers Surg. Med. **43**(2), 122–129 (2011).
10. W. J. Choi, H. Wang, and R. K. Wang, "Optical coherence tomography microangiography for monitoring the response of vascular perfusion to external pressure on human skin tissue," J. Biomed. Opt. **19**(5), 056003 (2014).
11. G. Liu, W. Jia, J. S. Nelson, and Z. Chen, "In vivo, high-resolution, three-dimensional imaging of port wine stain microvasculature in human skin," Lasers Surg. Med. **45**(10), 628–632 (2013).
12. L. V. Wang, "Prospects of photoacoustic tomography," Med. Phys. **35**(12), 5758–5767 (2008).
13. J. T. Oh, M. L. Li, H. F. Zhang, K. Maslov, G. Stoica, and L. V. Wang, "Three-dimensional imaging of skin melanoma in vivo by dual-wavelength photoacoustic microscopy," J. Biomed. Opt. **11**(3), 034032 (2006).
14. C. P. Favazza, O. Jassim, L. A. Cornelius, and L. V. Wang, "In vivo photoacoustic microscopy of human cutaneous microvasculature and a nevus," J. Biomed. Opt. **16**(1), 016015 (2011).

#241304 Received 19 May 2015; revised 9 Jul 2015; accepted 21 Jul 2015; published 31 Jul 2015

15. J. Aguirre, M. Schwarz, D. Soliman, A. Buehler, M. Omar, and V. Ntziachristos, "Broadband mesoscopic optoacoustic tomography reveals skin layers," Opt. Lett. **39**(21), 6297–6300 (2014).
16. J. J. Niederhauser, M. Jaeger, R. Lemor, P. Weber, and M. Frenz, "Combined ultrasound and optoacoustic system for real-time high-contrast vascular imaging in vivo," IEEE Trans. Med. Imaging **24**(4), 436–440 (2005).
17. G. Held, S. Preisser, H. G. Akarçay, S. Peeters, M. Frenz, and M. Jaeger, "Effect of irradiation distance on image contrast in epi-optoacoustic imaging of human volunteers," Biomed. Opt. Express **5**(11), 3765–3780 (2014).
18. E. Zhang, J. Laufer, and P. Beard, "Backward-mode multiwavelength photoacoustic scanner using a planar Fabry-Perot polymer film ultrasound sensor for high-resolution three-dimensional imaging of biological tissues," Appl. Opt. **47**(4), 561–577 (2008).
19. J. Laufer, F. Norris, J. Cleary, E. Zhang, B. Treeby, B. Cox, P. Johnson, P. Scambler, M. Lythgoe, and P. Beard, "In vivo photoacoustic imaging of mouse embryos," J. Biomed. Opt. **17**(6), 061220 (2012).
20. E. Z. Zhang, B. Povazay, J. Laufer, A. Alex, B. Hofer, B. Pedley, C. Glittenberg, B. Treeby, B. Cox, P. Beard, and W. Drexler, "Multimodal photoacoustic and optical coherence tomography scanner using an all optical detection scheme for 3D morphological skin imaging," Biomed. Opt. Express **2**(8), 2202–2215 (2011).
21. M. Liu, B. Maurer, B. Hermann, B. Zabihian, M. G. Sandrian, A. Unterhuber, B. Baumann, E. Z. Zhang, P. C. Beard, W. J. Weninger, and W. Drexler, "Dual modality optical coherence and whole-body photoacoustic tomography imaging of chick embryos in multiple development stages," Biomed. Opt. Express **5**(9), 3150–3159 (2014).
22. B. Hermann, M. Liu, N. Schmitner, B. Maurer, D. Meyer, W. J. Weninger, and W. Drexler, "Hybrid ultrahigh resolution optical coherence / photoacoustic microscopy," in *Proceeding of SPIE 9323, Photons Plus Ultrasound: Imaging and Sensing 2015*, A. Oraevsky, L. Wang, eds. (SPIE, 2015), 9323N.
23. "American National Standard for Safe Use of Lasers," American National Standards Institute **ANSI Z136.1** (2007).
24. B. E. Treeby and B. T. Cox, "k-Wave: MATLAB toolbox for the simulation and reconstruction of photoacoustic wave fields," J. Biomed. Opt. **15**(2), 021314 (2010).
25. J. Schindelin, I. Arganda-Carreras, E. Frise, V. Kaynig, M. Longair, T. Pietzsch, S. Preibisch, C. Rueden, S. Saalfeld, B. Schmid, J.-Y. Tinevez, D. J. White, V. Hartenstein, K. Eliceiri, P. Tomancak, and A. Cardona, "Fiji: an open-source platform for biological-image analysis," Nat. Methods **9**(7), 676–682 (2012).
26. P. McKee, *Pathology of the Skin with Clinical Correlations* (Mosby-Wolfe 1996).
27. S. Standring, *Gray's Anatomy, The Anatomical Basics of Clinical Practice* (Elsevier, 2005) Chap. 1.
28. I. M. Braverman, "The cutaneous microcirculation," J. Investig. Dermatol. Symp. Proc. **5**(1), 3–9 (2000).
29. H. Gray, *Anatomy of the Human Body* (Bartleby, 2000).
30. E. B. Brown, R. B. Campbell, Y. Tsuzuki, L. Xu, P. Carmeliet, D. Fukumura, and R. K. Jain, "In vivo measurement of gene expression, angiogenesis and physiological function in tumors using multiphoton laser scanning microscopy," Nat. Med. **7**(7), 864–868 (2001).

1. Introduction

The vascular network of the skin reflects the tissue's health, with its alterations exhibiting a characteristic disease imprint. Clinical examinations using dermoscopy and histopathology are considered the gold standard for diagnosis [1]. However, visualization of the tissue's vascular network, which provides insight into the metabolic demand of a skin disease and helps us understand the pathology, is limited with these procedures. Visualizing vascular patterns can lead to improved identification of inflammatory skin diseases and skin cancer, where vascular density and arborized structures provide valuable information on the diseases' severity and progression [2]. In addition, vascular patterns could be used to monitor treatment effectiveness [3].

Previously, magnetic resonance imaging (MRI) was used to image the vessels in the superficial vascular plexus and deep vascular plexus of the human thigh *in vivo*, with an acquisition time of 10 min 7 s [4]. In the data sets, the vessels were manually segmented and a 3D vascular network was presented. Vessels and morphology were visualized at depths up to several millimeters, and anatomical features such as pilosebaceous units and hair follicles are visible on the images. However, with an isotropic spatial resolution of 100 μm, the system used by Laistler et al. [4] could distinguish only the epidermis and dermis and could not show detailed morphologies. The poor resolution of MRI inhibits its application in dermatology.

Optical coherence tomography (OCT), with its superior spatial resolution compared to that of MRI, has been widely accepted as a novel imaging modality in dermatology in the last decade [5]. Being a noninvasive, nonionizing and cost effective technique, boasts its translation into the clinics for dermatological studies [6, 7]. Combining OCT with other imaging modalities, such as multiphoton tomography (MPT) [8], could extend its dermatological applications even further.

#241304 Received 19 May 2015; revised 9 Jul 2015; accepted 21 Jul 2015; published 31 Jul 2015

While conventional OCT in dermatology is used to visualize the morphology, visualization of the vascular network using functional OCT has been investigated by various groups. We can obtain functional images of the skin and visualize the microvasculature by analyzing the differences in the intensity on successive OCT tomograms [2]. Imaging of microcirculation under psoriatic conditions, using ultrahigh-sensitive optical microangiography (UHS-OMAG) was reported by Qin et al. [9]. The OMAG as a recent extension of OCT has been used to monitor vascular perfusion in the nail fold [10]. Doppler OCT (DOCT), another functional extension of OCT, has been used for imaging microvasculature as well [11]. It differentiated the microvasculature mesh between pathological tissue and healthy tissue in a patient with port wine stain [11]. OCT-based techniques have a great capacity for dermatological imaging, with focus on morphology and vasculature. However, their effective penetration depth for vasculature visualization does not exceed the optical transport mean free path, which is about 1 mm in human skin [12].

Photoacoustic imaging (PAI) is a relatively new technique with an imaging depth beyond the transport mean free path; its biomedical applications are progressively emerging. In particular, the strong optical absorption of endogenous hemoglobin provides opportunities for the assessment of skin conditions characterized by microvascular abnormalities. Photoacoustic microscopy (PAM) with an ultrasound transducer-based setup has been used for imaging cutaneous microvasculature and skin melanoma [13]. Favazza et al. [14] used dual-wavelength PAM to image vasculature and a common blue nevus. They reported on the visualization of capillaries in the dermal papillae as well as the subpapillary plexus in a healthy subject. Aguirre et al. [15] reported on the application of an ultra-broadband transducer (20–200 MHz) in a photoacoustic tomography (PAT) system to visualize skin layers, capillary mesh, and the blood vessel plexus. Although the system differentiated the dermis–epidermis layers, lack of contrast of PAI for imaging any structural morphology such as sweat ducts or pathology in the skin, necessitates use of other imaging modalities for dermatological applications.

The combination of photoacoustic and ultrasound imaging has shown great potential in the clinical setting [16]. Using a transducer array, both modalities can be integrated in a hand-held probe. While photoacoustic imaging visualizes vessels up to 10 mm depth from the surface of the skin, ultrasound B-mode imaging visualizes anatomical parts such as bone and fascia [17]. However, in their combined system, due to the lack of contrast of ultrasound imaging, the morphology of the skin cannot be visualized.

Among the various modalities for *in vivo* imaging of vasculature, the PAT system with a planar sensor [18] has a deep imaging depth and can be combined with other modalities. Laufer et al. [19] achieved *in situ* imaging of mouse embryo vasculature to a depth of 10 mm. Zhang et al. [20] used the combined PAT/OCT to image a healthy human subject with the images of the submodalities inherently coregistered. Liu et al. [21] with a similar combined PAT/OCT system provided complementary information with clinical relevance from imaging a chick embryo *ex ovo*. A recent review article [7] has shown several different types of PAM/OCT systems. The representative designs of PAM/OCT employ either an obliquely positioned unfocused ultrasound transducer to clear the field of view for laser scanning, or a focused transducer but with limited field of view [22]. These implementations have either low sensitivity, or low speed. In many cases, the need for a bulky water tank also limits PAM/OCT systems in clinical applications. In the contrary, the presented PAT/OCT system requires no water tank and the backward mode operation permits easy adaptation for patient imaging. In addition, the long penetration depth achieved by the PAT system, which is not available by normal PAM configurations [7], is a necessity for dermatological research that requires visualization of vasculature several millimeters below the skin surface.

To perform *in vivo* studies on the human hand, we developed an imaging head that expands the spectrum of applications for our dual modality PAT/OCT system. The imaging head is independent of the optical table and can be placed at the proper height next to a patient chair while the patient sits in the chair.

#241304 Received 19 May 2015; revised 9 Jul 2015; accepted 21 Jul 2015; published 31 Jul 2015

We present the results of our dual-modality PAT/OCT system used for the first time to image palms with healthy and diseased skin. Various skin pathologies were imaged to demonstrate the diverse range of diseases that this system can monitor. We recruited 16 patients with inflammatory skin diseases, including atopic dermatitis, chronic hyperkeratotic hand eczema, and dyshidrotic hand eczema. The vascular networks of these diseases were compared with those of normal skin as a control.

2. Materials and methods

The 16 patients imaged in this study were recruited from the Department of Dermatology, Medical University of Vienna. In addition, we imaged eight healthy volunteers. The exact same location on the palm was imaged for all the subjects, so that it was possible to compare the images. That is the skin on top of the abductor pollicis brevis in the thenar eminence, indicated with a blue square in Fig. 1(b). The study was approved by the ethics committee of the Medical University of Vienna and followed good scientific and clinical practices as well as the Declaration of Helsinki.

Figure 1(a) shows the schematic of the multimodal system. Descriptions of the swept-source OCT and the excitation setups were given in detail in our previous publication [21] and the PAT interrogation in [18]. For this study the benchtop scan unit used in the previous system was redesigned and modified into a new imaging head whose footprint is 540 cm^2 (84 in^2) and is independent of the optical table, as shown in Fig. 1(c). The light for excitation, interrogation and OCT are coupled via optical fibers. The imaging head was placed at the proper height next to the patient chair so that the subject could easily place the palm on the Fabry–Pérot interferometer (FPI) sensor head. Figure 1(d) shows the hand of a subject on the FPI while being imaged.

The OCT light source was centered at 1060 nm and had a bandwidth of 100 nm. The sensitivity of the OCT system was 94 dB. The power of the OCT beam on the sample was 4.8 mW and the lateral and axial resolutions of the system were 20 μm and 5 μm, respectively.

The pulse repetition frequency (PRF) of the PAT pump laser was 50 Hz. The output of OPO was set at 650 nm and energy of 30 mJ. The coupling efficiency of the multimode fiber was 80% and hence the energy at its output tip was 24 mJ. The fiber tip was positioned several centimeters away from the FPI sensor so that the illuminated area on top of the FPI was a circle with diameter of 2 cm. The excitation beam passed through the FPI sensor and underwent attenuation (absorption by the FPI sensor substrate and reflection by the surface of the FPI). The incident fluence measured on top of the FPI sensor was 3.1 mJ/cm^2, in compliance with the ANSI safety limit of skin exposure for pulse train with illumination time more than 10 s and the given PRF. [23]. The output of the interrogation laser was set to 8.3 mW and the power of the incident beam on the FPI was 5.4 mW. A 1951 USAF resolution test target, placed 2.9 mm from the FPI sensor, was used to measure the resolution. The lateral and axial resolutions of the system were 157 μm and 42 μm, respectively. The axial resolution is independent of the location of the resolution target; however, the lateral resolution is location dependent, for detailed description please refer to [18]. The measured resolution values are representative for the central region of the imaged area at the aforementioned depth. Distilled water was used as the acoustic couplant for PAT imaging.

The scanned area was 14.16 mm × 14.16 mm for both modalities. The lateral step size during acquisition was 10 μm for OCT and 120 μm for PAT. The digitizer used for PAT acquisition was set at 250 MS/s and at each acquisition point one waveform of 1200 points was recorded. The acquisition time was 20 s for OCT and 4 min 39 s for PAT. The PAT acquisition time is defined by the PRF of the pump laser. The overall dual-modality imaging time was 7 min 30 s for all subjects in this study. The overall time consists of acquisition and transfer of the raw data from the memory to the hard disk for each modality and switching between the OCT and PAT mode. Neither averaging nor motion artifact correction were applied. PAT interrogation and OCT beams share the same path between the flip mirror [Fig. 1(a)] and surface of the FPI; therefore the dual-modality volumes are inherently co-registered.

#241304 Received 19 May 2015; revised 9 Jul 2015; accepted 21 Jul 2015; published 31 Jul 2015

MATLAB 2010a (MathWorks, Natick, MA, USA) was used for post-processing and reconstruction of the OCT images. The PAT image reconstruction was performed using the k-Wave MATLAB toolbox [24]. Time-reversal reconstruction was used as the reconstruction scheme. Next, the reconstructed volumetric OCT and PAT data were spatially resampled and fused in Fiji [25] and the 3D-rendered videos and single frames were produced using CINEMA 4D (MAXON Computer GmbH, Friedrichsdorf, Germany).

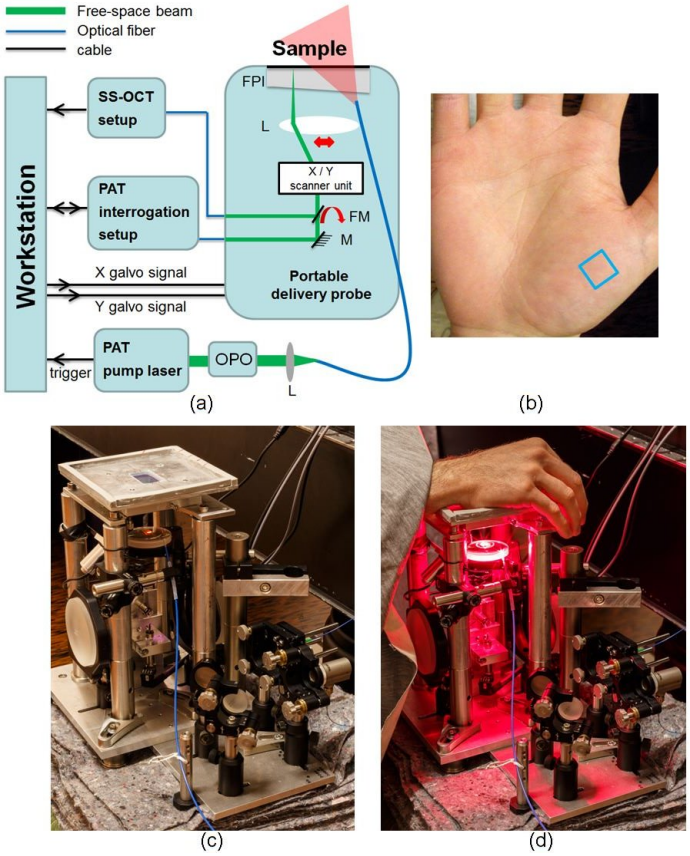

Fig. 1. (a) Schematic of the multimodal setup, L: scan lens, M: mirror, FM: flip mirror, FPI: Fabry–Pérot interferometer sensor head. (b) Photograph of a palm, the imaged area is indicated by a blue square. (c) Photograph of imaging head. (d) Imaging head with the subject's hand placed on the FPI and the excitation light incident on the palm.

3. Results

3.1 Healthy subjects

The PAT images of one subject are shown in Fig. 2. Figure 2(a) is a single frame from the 3D-rendered PAT data (video available at Visualization 1) and Fig. 2(b) presents a diagram of skin layers with corresponding vascular network (adapted from [26]), and *en face* PAT maximum intensity projection (MIP) images of the same data as in (a). Each panel is integration over a certain depth range, showing the vascular network in the papillary dermis (red frame), the superficial vascular plexus (green frame), the deep vascular plexus (blue frame), and the subcutaneous fat (yellow frame). The depth range for each MIP is given on the top of each panel. The two plexuses arise from the subcutaneous vessels and are connected by interconnecting vessels. The superficial vascular plexus, which is located in the papillary dermis, supplies the capillary loop system. These capillaries run along the ridges of

#241304 Received 19 May 2015; revised 9 Jul 2015; accepted 21 Jul 2015; published 31 Jul 2015

the papillary dermis. Most of the blood is directed to the more metabolically active parts of the skin, i.e., epidermis, hair papillae, and adnexal structures [the latter two are not visible in the diagram in Fig. 2(b)]. Capillary loops deliver the nutrition to the epidermis by diffusion [27]. The vessels in the papillary dermis consist of terminal arterioles, arterial and venous capillaries, and post-capillaries venules [26]. These vessels have diameters ranging from 4 μm to 35 μm [28] which are far below the resolution of the PAT system. Therefore, individual vessels are not discernible in the PAT images, in particular the majority of the vessels in the superficial vascular plexus [Fig. 2(b), green frame]. Few vessels seen mostly in the top-right corner of the green frame are the interconnecting vessels, which can be traced to the vessels in the deep vascular plexus. However, because of the amount of blood the capillary loop system contains, it is visualized as parallel curves coinciding with the curves of the epidermal ridges [29].

The 3D-rendered video of the fused PAT/OCT data is available in the supplementary material (Visualization 2). Figure 3 is a single frame from the video in which the PAT data is shown with the red colormap and the OCT data with the gold colormap. In this image, the surface of the epidermis, a part of the papillary dermis, and the capillaries in the papillary dermis are seen. A virtual cutout of the volume that moves in the depth direction shows the morphology of healthy skin and the distribution of the vessels in each layer.

To show the anatomical variations in the distribution of the vascular network among subjects, MIPs of the capillary loop system, deep vascular plexus, and the subcutaneous vessels for three different subjects are given in Fig. 4. The depth range for each panel is indicated on the top of the panel. As can be seen in the top row, the density of the curves, which directly corresponds to the density of the ridges of the papillary dermis, is slightly different among the subjects. The middle row shows the vessels in the deep vascular plexus and the interconnecting vessels. The vessel density inhomogeneity across the subjects is more pronounced in the middle row. In these images, the vessels can be grouped in two types of smaller and larger vessels. By looking at the volumetric data, it is observed that the larger vessels lie deeper in respect to the smaller vessels. These smaller vessels are mostly interconnecting vessels. The average diameter of the larger and smaller vessels is 890 μm and 200 μm, respectively. The bottom shows the subcutaneous vessels. The average diameter of these vessels is about 340 μm. The density of the subcutaneous vessels in comparison to the deep vascular plexus is lower in all the subjects. The reason that the depth range in which the subcutaneous vessels is positioned varies across the subjects could be related to the thickness of the subcutaneous fat layer in each subject.

#241304 Received 19 May 2015; revised 9 Jul 2015; accepted 21 Jul 2015; published 31 Jul 2015

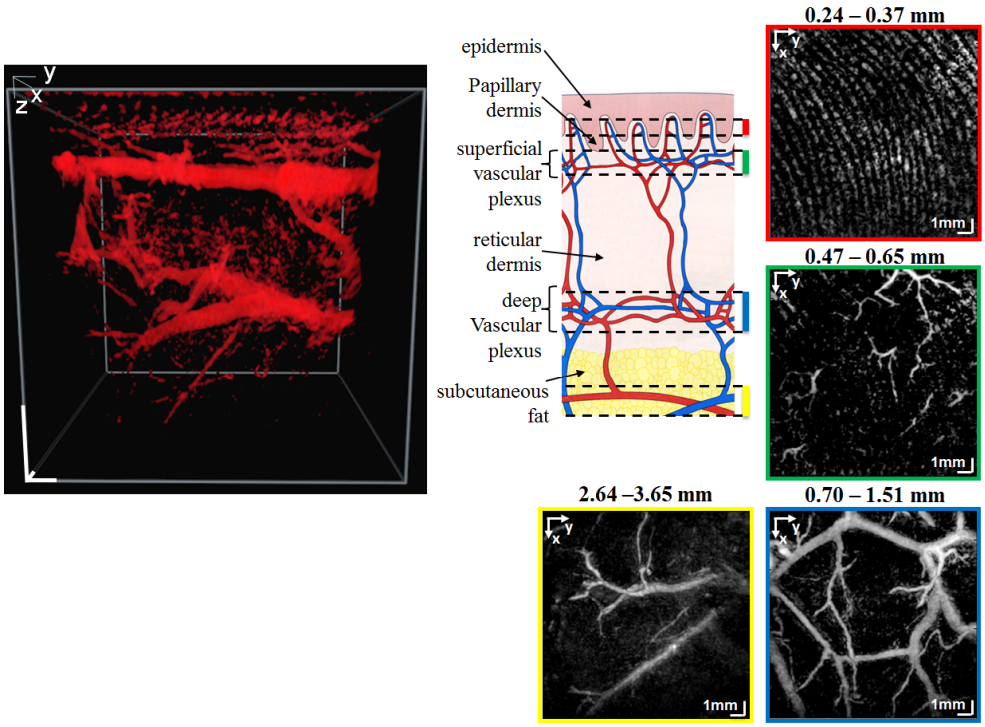

Fig. 2. (a) Single frame from the 3D-rendered volume of the PAT data showing the vasculature of a healthy subject (video available at Visualization 1). scale bars: 1 mm (b) Diagram of skin layers and vascular network (adapted from [26]) and MIP images calculated from the four depth ranges from the volume in (a) showing the vasculature in the papillary dermis (red frame), superficial vascular plexus (green frame), deep vascular plexus (blue frame), and subcutaneous vessels (yellow frame). Because of the resolution limitation of the system, the individual vessels of the capillary loop system and the superficial vascular plexus (diameter ranging from 4 μm to 35 μm) are not discerned. Few vessels seen mostly in the top-right portion of the green frame are the interconnecting vessels.

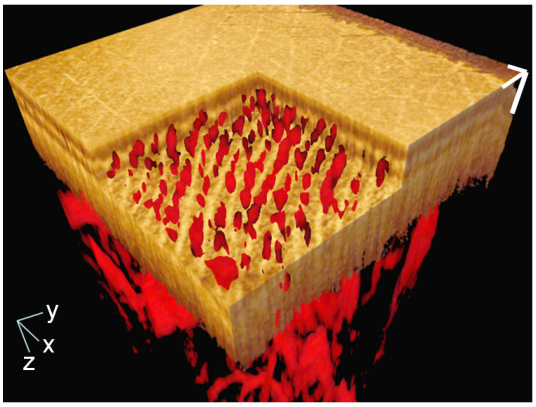

Fig. 3. Single frame from the 3D-rendered video of the fused PAT/OCT data from a healthy subject (video available at Visualization 2). The OCT data is presented with the gold colormap and the PAT data with the red colormap. The virtual cutout shows the capillary loop system in the papillary dermis. The PAT data is the same as in Fig. 2. The *x*- and *y*-axis scale bars: 1 mm; *z*-axis scale bar: 200 μm.

#241304 Received 19 May 2015; revised 9 Jul 2015; accepted 21 Jul 2015; published 31 Jul 2015

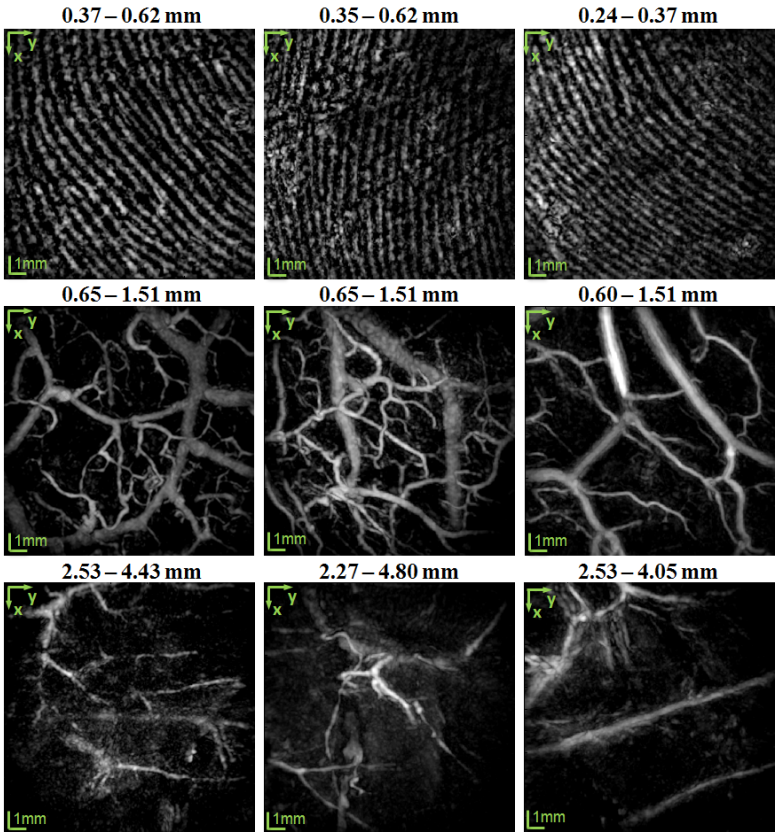

Fig. 4. MIP PAT images of three healthy subjects (columns). The rows from top to bottom represent the vascular distribution in the dermal papillae, mid- and deep dermis, and subcutaneous fat layer, respectively. Images in each column are of one subject. The vessels in the dermal papillae are organized into the capillary loop system and are visualized as parallel curves. In the middle row, the vessels are grouped according to size, with the smaller vessels having an average diameter of 200 μm and the larger vessels having an average diameter of 890 μm. The smaller vessels are mainly the interconnecting vessels. The average diameter of the subcutaneous vessels is 340 μm.

3.2 Chronic hyperkeratotic hand eczema

Chronic hyperkeratotic hand eczema manifests itself as thick areas of scale on the palm and can be difficult to distinguish from psoriasis. It is categorized as an inflammatory reaction of the skin that includes erythema, edema, papules, and crusting of the skin as well as epidermal lichenification. Its cause is unknown and it can be completely refractory to treatment.

Figure 5(a) shows the MIP PAT of the capillary loop system of a patient, where it can be seen that the demarcation between the curves of the capillary loop system is significantly smaller than that of healthy subjects. The space between adjacent curves is filled mostly with capillaries (compare with the first row of Fig. 4). The color-coded MIP of the PAT data [Fig. 5(b)] shows that the depth range (1.5–2.5 mm) between the lower reticular dermis and the subcutaneous fat interface exhibits extremely increased vascularization due to neo-angiogenesis. A single frame from the 3D-rendered video is given in Fig. 5(c). The volumetric data show that there is no longer any demarcation between the capillary loop system and the deep vascular plexuses. To increase the visibility in Figs. 5(b) and 5(c), the initial 380 μm is truncated. Figure 5(d) is a single frame from the 3D-rendered fused PAT/OCT data, with a virtual cutout depicting the surface of the epidermis, a part of the capillary loop system, and the papillary dermis.

#241304 Received 19 May 2015; revised 9 Jul 2015; accepted 21 Jul 2015; published 31 Jul 2015

The pathology of the subject of Fig. 5 manifests itself as high vascular proliferation. To better interpret the results, the MIP from a representative healthy subject covering a depth range of 1.5–2.5 mm is shown in Fig. 6(a), and Figs. 6(c) and 6(d) show the OCT cross-sectional images. The OCT images point out another feature of the disease: an 82% increase in the thickness of the epidermis compared to that of the healthy subject. These results demonstrate the capabilities of the multimodal system. Different diagnostic information can be extracted from the data depending on the contrast mechanism of each submodality: OCT is used to assess the skin layers and PAT the vascular network.

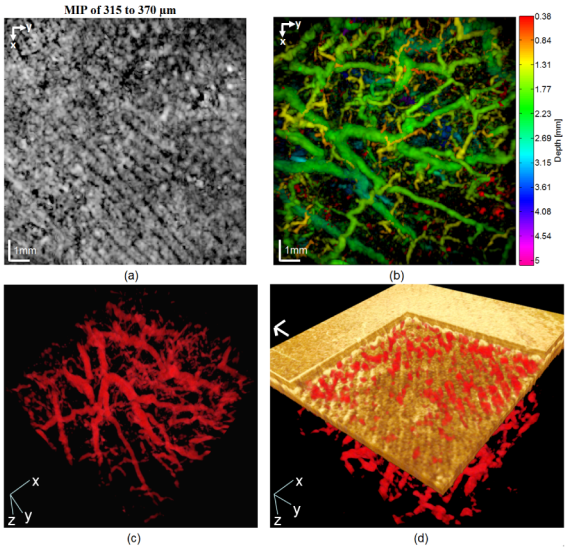

Fig. 5. (a) MIP PAT image of the capillary loop system of a patient with chronic hyperkeratotic hand eczema. (b) Color-coded MIP of PAT data. Notice the high degree of vascularization in the depth range of 1.5–2.40 mm. (c) Single frame from a 3D-rendered video of the PAT data (video available at Visualization 3). (d) Single frame from the 3D-rendered fused PAT/OCT data (video available at Visualization 4). In (d), *x*- and *y*-axis scale bars: 1 mm; *z*-axis scale bar: 200 µm.

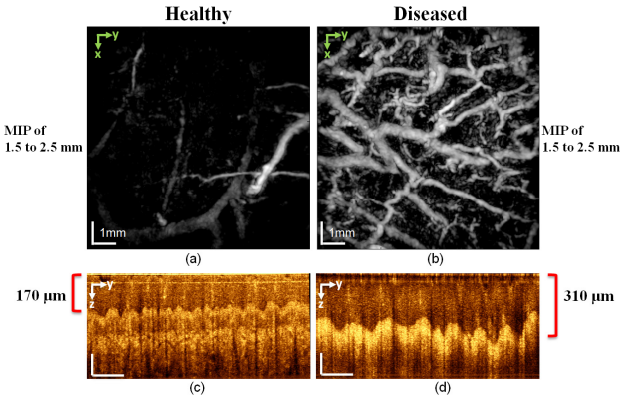

Fig. 6. Comparison of PAT and OCT images of a healthy subject (left column) and a diseased patient (right column) with chronic hyperkeratotic hand eczema. (a) and (b) MIP PAT integrating the depth range between 1.5 and 2.5 mm. This depth range includes the deeper vessels of the deep vascular plexus in the lower reticular dermis as well as few vessels arising from the superficial layer of the subcutaneous fat. Note the hypervascularization in the diseased subject. (c) and (d) OCT cross-sectional images show that the epidermis is thicker in the diseased patient than in the healthy subject. In (c) and (d), vertical scale bars: 100 µm; horizontal scale bars: 1 mm.

#241304 Received 19 May 2015; revised 9 Jul 2015; accepted 21 Jul 2015; published 31 Jul 2015

3.3 Chronic hand eczema under treatment

Figure 7 compares the PAT images of a healthy subject (left column) with those of a patient diagnosed with chronic hand eczema. The patient had applied topical steroids, known for its antiproliferative and vasoconstrictive effects, for 24 months prior to the imaging session.

The top panels show the MIP of the vasculature in the mid to lower reticular dermis, covering the depth range of 0.5–1.2 mm. For the healthy subject, the smaller vessels at the shallower part of the deep vascular plexus are visible. The bottom panels cover the depth range of 1.2–3.0 mm and show the larger vessels in the deep vascular plexus located in deeper part of the reticular dermis, and the superficial part of the subcutaneous tissue. For the diseased patient, the reduced number of vessels is indicated by the sparse vascular network in deep vascular plexus.

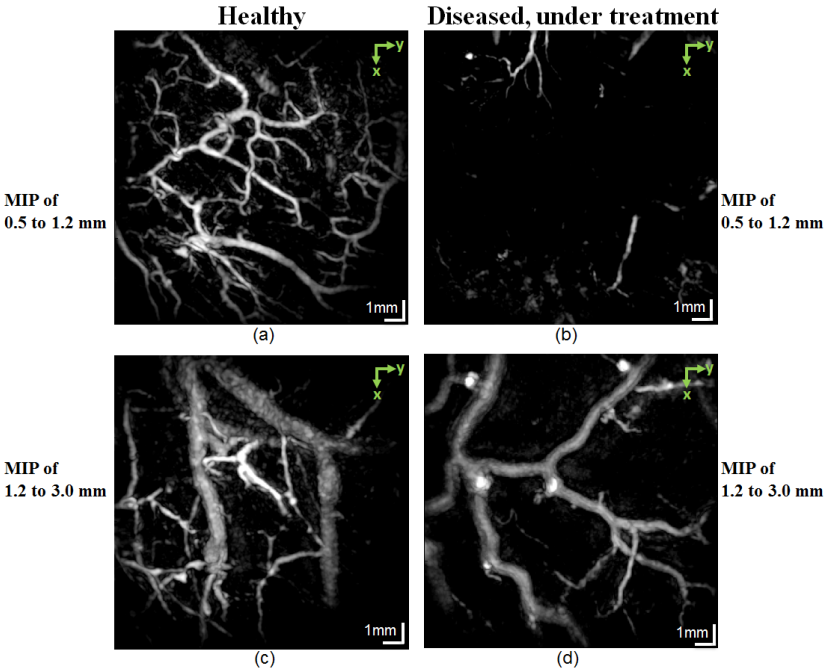

Fig. 7. Comparison of PAT images of a healthy subject (left column) and a patient with chronic hand eczema under treatment (right column). (a) and (b): MIP PAT integrating the depth range between 0.5 and 1.2 mm. For the healthy subject, the smaller vessels in the shallower part of the deep vascular plexus are seen. (c) and (d) Integrating the depth range between 1.2 and 3.0 mm show the larger vessels in the deeper part of the deep vascular plexus and the part of the vessels arising from the subcutaneous fat layer. Because of the antiproliferative and vasoconstrictive effects of the topical steroid used by the diseased patient, the vascular network is sparse.

3.4 Dyshidrotic hand eczema

The main symptom of dyshidrotic hand eczema is the development of vesicles on the fingers and palms. They are extremely itchy and form painful, scaly patches of skin that get red and burst. Scratching causes skin changes and thickening. The exact cause of the disease is unknown but stress, allergies such as hay fever, and often contact of the skin with water can trigger the disease.

The MIP PAT images of this disease are presented in Fig. 8, where each panel is a MIP calculated over the depth range displayed next to each panel. The imaged area was on top of a red patch with fresh scar tissue where healing was in progress. Figure 8(a) shows the signal from the papillary dermis. The curves of the normal-looking capillary loop system are seen in

#241304 Received 19 May 2015; revised 9 Jul 2015; accepted 21 Jul 2015; published 31 Jul 2015

the lower right but are not visible in the left side of the figure. Figures 8(b) and 8(c) present the vessels in the deep vascular plexus. As for the healthy cases, the smaller vessels in this plexus are shallower than the larger vessels. Figure 8(d) shows the subcutaneous vessels.

Figures 9(a) and 9(b) present *en face* OCT images at different depths of the same scanned area as in Figs. 8. The left part of Fig. 9(a) shows the scar tissue, which clearly differs in texture from the healthy tissue on the right, in which the ridges of the papillary dermis and sweat ducts are visible. Figure 9(b) shows the texture difference and demarcation between the scar tissue and the healthy tissue in the reticular dermis at a depth of 520 μm. It is clinically expected that the pathology continues to deeper depth; however, the contrast on the OCT images decreases dramatically in deeper depth. Figures 9(c) and 9(d) are PAT and fused PAT/OCT images, respectively. The PAT image shows the smaller vessels of the deep vascular plexus. In the fused image, the diameter of the vessels at the border of the scar tissue is reduced. The auto-coregistered complementary information obtained from each submodality is essential for interpreting the images. Figure 10(a) presents *en face* OCT image. To assess the extent of the changes to the skin caused by the pathology, we compared an OCT cross-sectional image from the scar tissue area [Fig. 10(b)] with that from a healthy site [Fig. 10(c)]. The lines along which the cross sections were taken are marked (with dashed lines 1 and 2) in the *en face* image. In the scar tissue portion of Fig. 10(b), the epidermis is significantly altered and its average thickness is reduced to 41 μm, whereas in Fig. 10(c), the thickness of the epidermis is relatively constant along the *x* axis and the average thickness is 140 μm. The spiral shape of sweat ducts also is noticeable in Fig. 10(c).

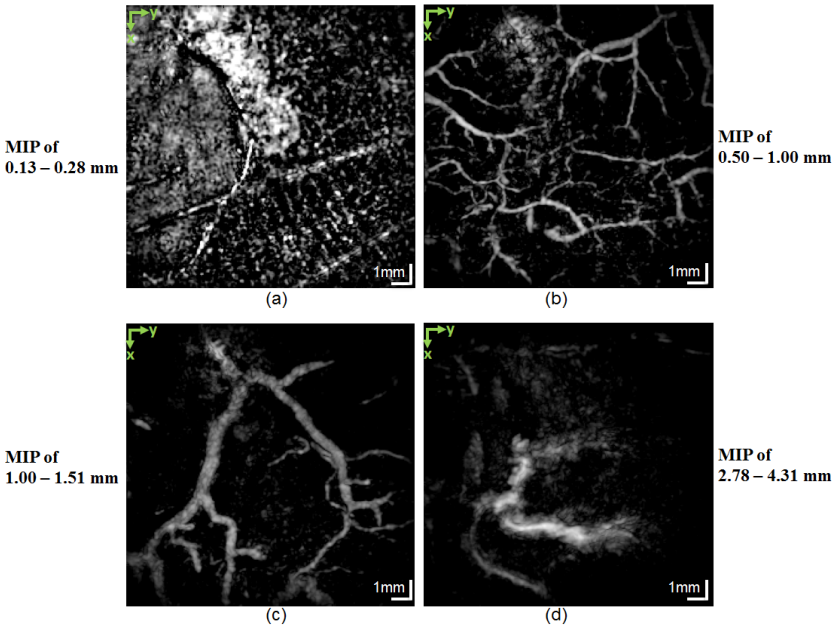

Fig. 8. *En face* MIPs from a patient suffering from dyshidrotic hand eczema taken at selected depths: (a) 0.13–0.28 mm, covering the papillary dermis depth range. The curves of the capillary loop system are visible on the bottom right-hand side but are gone on the left-hand side. (b) 0.5–1.0 mm, covering the smaller vessels in the deep vascular plexus; (c) 1.0–1.5 mm, covering the larger vessels in the deep vascular plexus; (d) 2.78–4.31 mm, covering the vessels in the subcutaneous fat tissue.

#241304 Received 19 May 2015; revised 9 Jul 2015; accepted 21 Jul 2015; published 31 Jul 2015

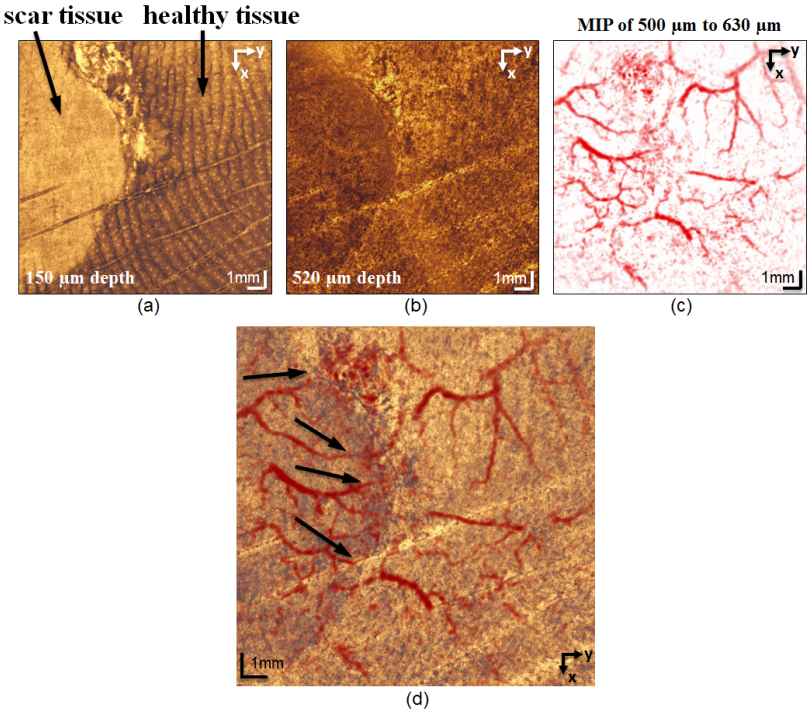

Fig. 9. Images from a patient with dyshidrotic hand eczema. (a) *En face* OCT images at a depth of 150 µm. The texture of the scar tissue on the left side of the image is distinctly different from the healthy tissue on the right. Ridges of the papillary dermis and the sweat ducts (bright spots) are visible. (b) *En face* OCT images at a depth of 520 µm. The border between the scar tissue and the healthy tissue is noticeable at this depth. (c) MIP PAT integrating the depth range 500–630 µm. (d) PAT images overlaid on OCT images. Notice the thinning of the vessels at the interface between the scar tissue and the heathy tissue (black arrows). The 3D-rendered video of the fused PAT/OCT data is available at Visualization 5.

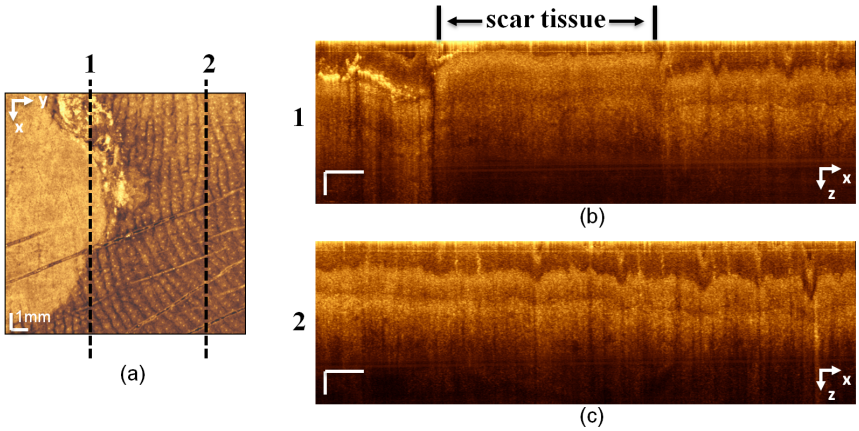

Fig. 10. (a) *En face* OCT image in which dashed lines 1 and 2 correspond to the cross-sectional images in (b) and (c), respectively. The cross section line 1 in (a) includes scar tissue and a portion of healthy tissue. On the cross-sectional image in (b), the thickness of the epidermis in the scar portion is significantly reduced and the morphology of the skin layers is altered. (c) The cross-sectional image of healthy tissue. The dermis–epidermis junction, sweat ducts, and the overall thickness of the epidermis, which is constant along the *x* axis, can be seen. *x*-axis scale bar: 1 mm; *z*-axis scale bar: 100 µm.

#241304 Received 19 May 2015; revised 9 Jul 2015; accepted 21 Jul 2015; published 31 Jul 2015

3.5 Atopic dermatitis

The etiology of atopic dermatitis is unknown. However, there is evidence that the disease occurs in individuals with a family history of allergies. The inflammation of the skin that causes the atopic dermatitis rash is considered a type of allergic response. The disease can be chronic or acute. Its major symptom is itchiness and scratching the affected areas causes a red, patchy rash. There is medication that can alleviate the itchiness and treat the rash.

An interesting result of this study was the detection of possible microaneurysms in the vasculature of a patient diagnosed with atopic dermatitis. Figure 11 displays the MIP PAT images of different depth ranges, which are indicated at the side of each panel. Figure 11(a) shows the capillary loop system and Fig. 11(b) shows the smaller vessels in the deep vascular plexus, which are not as deep as the larger vessels in this plexus. Figure 11(c) presents the larger vessels of the deep vascular plexus and the vessels arising from the subcutaneous tissue. The subcutaneous vessels are shown in Fig. 11(d). To understand better the vascular distribution in this data set, color-coded depth information MIP of the PAT data is given in Fig. 12(a). Figures 12(b) and 12(c) are enlargements of areas containing the possible microaneurysms.

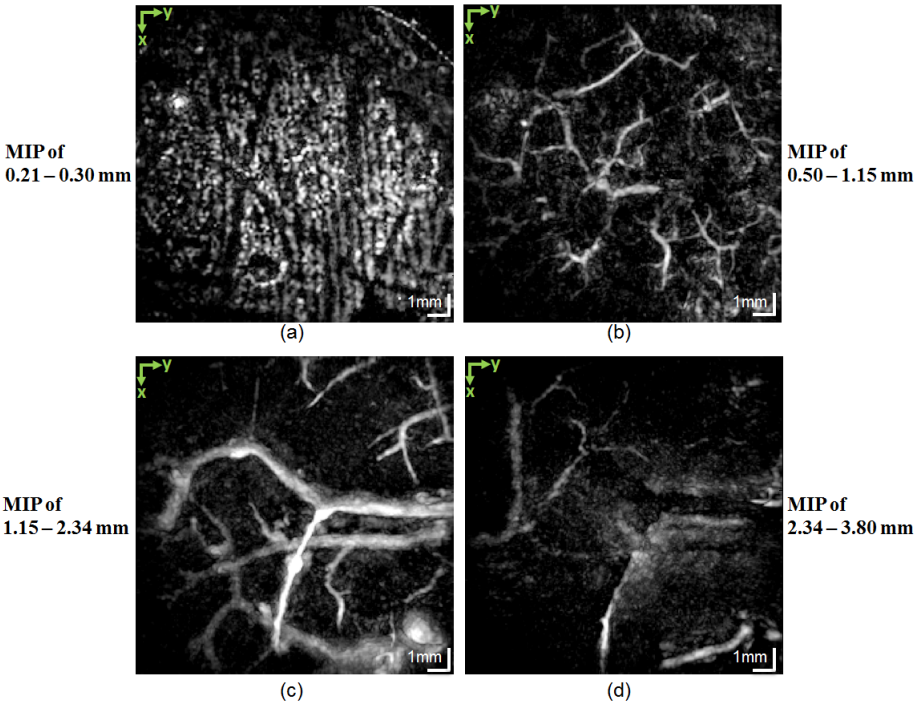

Fig. 11. MIP PAT images of atopic dermatitis. (a) Integration of the depth range of 0.21–0.30 mm shows the capillary loop system in the papillary dermis; (b) the smaller vessels in the deep vascular plexus; (c) the larger vessels in the deep vascular plexus and part of the vessels arising from the subcutaneous tissue; (d) the subcutaneous vessels. Possible microaneurysms are detected in (c). The enlarged views are given in Fig. 12.

#241304 Received 19 May 2015; revised 9 Jul 2015; accepted 21 Jul 2015; published 31 Jul 2015

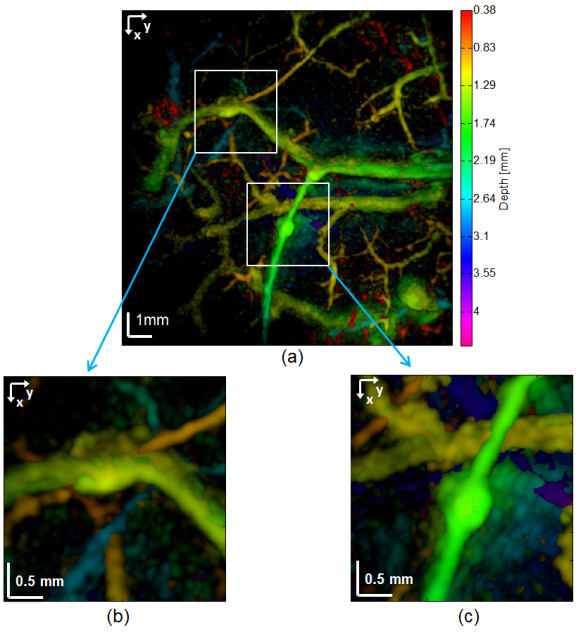

Fig. 12. MIP PAT images of atopic dermatitis. (a) Color-coded depth information. The colorbar on the right shows the depth in millimeters for each color tone. (b) and (c) Enlarged view of two possible aneurysms.

4. Discussion

The complementary information of PAT and OCT in their overlapping imaging depth range provides valuable information to clinicians. For instance, for dyshidrotic hand eczema, while OCT visualizes the scar tissue and its interface with healthy tissue in the epidermis and dermis, PAT shows the change in the vasculature at the edge of the scar tissue. This complementary information, which relates the change in morphology with the abnormality in the vasculature, is clinically useful for assessing the scar tissue and providing more insight into the healing process of such tissue. In addition to this examples, which demonstrates the complementary nature of the information in the overlapping depth range, imaging the vasculature at deeper depths than the OCT can penetrate would assist dermatological diagnosis and treatment monitoring. This is particularly advantageous in the study of angiogenesis in skin cancer.

Comparison of vasculature distribution in patients with chronic hyperkeratotic hand eczema with that of healthy subjects reveals an increased vascularization due to neo-angiogenesis that results from the tissue's strong metabolic requirements [30]. The diseased skin lesion shows vascular patterns that are significantly different from healthy skin, with dilated vessels in an unorganized network. The dermis tissue in patients with this disease has a high degree of scattering in comparison to healthy subjects; this could be related to the hyperkeratosis aspect of the disease. This scattering limits the penetration depth of the OCT beam, thus reducing the visibility of features in the deeper dermis. However, the enhanced scattering could be used as an additional diagnostic marker in assessing the tissue's condition.

Comparison of the PAT images of a representative healthy subject with those of a patient with chronic hand eczema under 24 months of treatment, showed reduced vascularization in the reticular dermis and superficial part of the subcutaneous tissue of the patient. The topical steroid that was used for the treatment manifested its effect as sparse vascular network. There are very few to no vessels visible in the upper reticular dermis. However it is suggested that due to limited resolution of the PAT images, it is not possible to draw any conclusion regarding the microvasculature.

#241304 Received 19 May 2015; revised 9 Jul 2015; accepted 21 Jul 2015; published 31 Jul 2015

Irregularities resembling aneurysms were noticed in the vascular structures of a nondiabetic patient with atopic dermatitis. The relationship between the skin's pathology and the possible aneurysms is not clinically known and further investigation is required.

The achievable resolution of the FPI based PAT setup is dependent upon a number of factors including the overall detection aperture, the effective element size, and the scan step size [18]. The spot size of the interrogation beam on the FPI sensor determines the effective element size. In the design of the dual-modality system, to have both OCT and PAT working, we used a long focal length achromatic doublet as the scan lens and therefore the interrogation beam spot size was 20 μm. However, since the PRF of the excitation laser is only 50 Hz, acquisition of a PAT data set that covers a large enough area would take tens of minutes, if we use 20 μm as the scan step size, which is against the goal of minimizing the imaging time for patients. Therefore we empirically chose 120 μm to be the scan step size so that a well-balanced tradeoff between the achievable resolution and imaging duration was reached.

The dermal papillae are highly vascularized and contain a network of capillary loops [27]. These capillaries direct the blood flow toward the epidermal tissue in their vicinity but they do not protrude into the epidermis. Individual capillaries are too fine to be discerned with PAT; however, the network that fills the papillary ridges can be seen in the PAT volumes as parallel curves running along the ridges, beneath the epidermis. We can also visualize this capillary network by using the functional extension of OCT, namely, angiography-OCT [2]. Acquisition of a typical angiography-OCT data set takes a few seconds. Combining angiography-OCT with PAT provides the possibility of having high resolution images of the capillaries in the shallower depth and the 3D vasculature network at deeper depth.

The imaging head in this study is not a hand-held device so its application in human studies is limited to imaging the palm. This does pose limitations on patient recruitment. A hand-held probe would facilitate the imaging of other parts of the body such as shoulders, back, and the lower extremities. Imaging the lower extremities is of particular interest because typically there are few if any motion artifacts caused by the beating heart and lung movement during imaging. Therefore, multimodal PAT/OCT imaging of pathologies on the lower extremities is less challenging. Various diseases such as diabetes manifest skin pathologies in the lower extremities. Thus, investigating the vascular network and the skin's morphology in such diseases using the multimodal PAT/OCT system would accelerate progress in related research.

Although 4 min 39 s of PAT acquisition time might seem too long to avoid motion artifact, in most of the cases no motion artifact was experienced. This is because of the ergonomic positioning of the palm on the imaging head next to the patient chair. While the arm and elbow of the subject were laid on the armrest of the chair, the palm was positioned on the FPI sensor without forcing any uncomfortable sitting posture.

In this study, each subject was imaged in one imaging session. However, it would be beneficial to perform a longitudinal study to monitor and assess the development of pathologies as well as the effectiveness of medications targeted to treat those pathologies.

5. Conclusions and future work

Patients with various skin pathologies and healthy subjects were imaged with our dual-modality PAT/OCT and coregistered volumetric images were obtained. Based on the endogenous contrast of the skin, OCT visualizes the skin's morphology and PAT shows the spatial distribution of the blood vessels. Vasculature plays an important role in many skin diseases. Multimodal PAT/OCT imaging of the vasculature can be a powerful tool in the study and monitoring of numerous dermatological diseases.

The visualization of the capillaries in the capillary loop system in the papillary dermis using coregistered multimodalities such as PAT/OCT will provide additional complementary information that is clinically relevant for several pathologies. We plan to incorporate angiography-OCT into the multimodal system to enable the imaging of these capillaries.

#241304 Received 19 May 2015; revised 9 Jul 2015; accepted 21 Jul 2015; published 31 Jul 2015

We demonstrated how the information from one modality complements and helps the interpretation of the data from another modality. This elegant tool for dermatological imaging of various pathologies is noninvasive and fast. Upon its successful translation to the clinic, the clinician can perform the measurements and then interpret and analyze the results during one visit by the patient.

Acknowledgments

We acknowledge the help of M. Bonesi, H. Sattmann, and C. Glittenberg. This project was funded by the Austrian Science Fund (project No. S10510-N20) and the European project FAMOS (project No. FP7 ICT 317744).

#241304 Received 19 May 2015; revised 9 Jul 2015; accepted 21 Jul 2015; published 31 Jul 2015